

Investigation of carbon dioxide photoreduction process in a laboratory-scale photoreactor by computational fluid dynamic and reaction kinetic modeling

Citation for published version:

Lu, X, Luo, X, Thompson, WA, Tan, JZY & Maroto-Valer, MM 2022, 'Investigation of carbon dioxide photoreduction process in a laboratory-scale photoreactor by computational fluid dynamic and reaction kinetic modeling', *Frontiers of Chemical Science and Engineering*, vol. 16, pp. 1149–1163.
<https://doi.org/10.1007/s11705-021-2096-0>

Digital Object Identifier (DOI):

[10.1007/s11705-021-2096-0](https://doi.org/10.1007/s11705-021-2096-0)

Link:

[Link to publication record in Heriot-Watt Research Portal](#)

Document Version:

Publisher's PDF, also known as Version of record

Published In:

Frontiers of Chemical Science and Engineering

Publisher Rights Statement:

© The Author(s) 2021.

General rights

Copyright for the publications made accessible via Heriot-Watt Research Portal is retained by the author(s) and / or other copyright owners and it is a condition of accessing these publications that users recognise and abide by the legal requirements associated with these rights.

Take down policy

Heriot-Watt University has made every reasonable effort to ensure that the content in Heriot-Watt Research Portal complies with UK legislation. If you believe that the public display of this file breaches copyright please contact open.access@hw.ac.uk providing details, and we will remove access to the work immediately and investigate your claim.

Investigation of carbon dioxide photoreduction process in a laboratory-scale photoreactor by computational fluid dynamic and reaction kinetic modeling

Xuesong Lu, Xiaojiao Luo, Warren A. Thompson, Jeannie Z.Y. Tan, M. Mercedes Maroto-Valer (✉)

Research Centre for Carbon Solutions, School of Engineering and Physical Sciences, Heriot-Watt University, Edinburgh EH14 4AS, UK

© The Author(s) 2021. This article is published with open access at link.springer.com and journal.hep.com.cn

Abstract The production of solar fuels via the photo-reduction of carbon dioxide to methane by titanium oxide is a promising process to control greenhouse gas emissions and provide alternative renewable fuels. Although several reaction mechanisms have been proposed, the detailed steps are still ambiguous, and the limiting factors are not well defined. To improve our understanding of the mechanisms of carbon dioxide photoreduction, a multi-physics model was developed using COMSOL. The novelty of this work is the computational fluid dynamic model combined with the novel carbon dioxide photoreduction intrinsic reaction kinetic model, which was built based on three-steps, namely gas adsorption, surface reactions and desorption, while the ultraviolet light intensity distribution was simulated by the Gaussian distribution model and Beer-Lambert model. The carbon dioxide photoreduction process conducted in a laboratory-scale reactor under different carbon dioxide and water moisture partial pressures was then modeled based on the intrinsic kinetic model. It was found that the simulation results for methane, carbon monoxide and hydrogen yield match the experiments in the concentration range of $10^{-4} \text{ mol} \cdot \text{m}^{-3}$ at the low carbon dioxide and water moisture partial pressure. Finally, the factors of adsorption site concentration, adsorption equilibrium constant, ultraviolet light intensity and temperature were evaluated.

Keywords carbon dioxide photoreduction, computational fluid dynamic simulation, kinetic model, Langmuir adsorption

1 Introduction

Atmospheric carbon dioxide (CO_2) mainly from combustion of fossil fuel is one of the major greenhouse gases and contributes about 60% to global warming [1]. To mitigate CO_2 emissions, the usage of fossil fuels should be decreased as well as deploying CO_2 capture, utilization and storage strategies. CO_2 utilization via photoreduction to methane (CH_4) is a promising method to produce solar fuels aiming at dealing with the problems of insufficiency of sustainable energy and reduction of CO_2 emissions [2,3].

However, the main obstacle for the CO_2 photoreduction to CH_4 process to be commercialised is its low conversion rate [4]. To address this challenge, understanding the mechanism and reaction kinetics is crucial for the improvement of the reaction efficiency [5]. The heterogeneous CO_2 photoreduction process includes the separation and recombination of electron-hole pairs in the semiconductor (photocatalyst), the gas adsorption and desorption on the surface of the photocatalyst, the electron and hole trapping reactions and the radical propagation reactions [6]. For the widely used photocatalyst TiO_2 , Qian et al. [7] reviewed charge carrier trapping, recombination and transfer, whereas Vorontsov et al. [8] reviewed its surface chemistry. In general, most of the kinetic models proposed for CO_2 photoreduction were based on the Langmuir-Hinshelwood equation and assumed adsorption and reaction as a one-step process [9]. For instance, Tahir and Amin [10] constructed the reaction kinetics of CO_2 photoreduction in a microchannel monolith photoreactor using the Langmuir-Hinshelwood reaction kinetic model. To account for apparent photocatalyst deactivation under continuous flow, Thompson et al. [11] introduced the Weibull possibility density function into the kinetic equation. Meanwhile, Marczewski [12] proposed a simple and easy integrated kinetic Langmuir model to analyze the

comprehensive reaction process. Bloh [13] built a kinetic model based on the generation of reactive surface sites, recombination of charge-carrier counterpart and charge transfer to the target substrate.

Computational fluid dynamic (CFD) modeling combining reaction kinetics is an effective tool to ascertain the reaction process [14]. Understanding the interactions between physical behavior and chemical reaction mechanism helps to determine the key parameters controlling the whole process and guides the future reactor design and scale-up. CFD studies have been reported to model different photoreactors, as discussed here: 1) A slurry bed photoreactor with ultraviolet (UV) lamps was used by Chu et al. [15] to model a new type of CO₂ photoreduction reactor, namely a twin reactor. 2) A packed bed or monolith reactor with optical fibers was modeled by Chen et al. [16] to investigate CO₂ photoreduction. 3) A thin-film flatbed reactor was modeled by Verbruggen et al. [17] for the degradation of gaseous acetaldehyde. However, this type of thin-film photoreactor has not been simulated for CO₂ photoreduction to CH₄.

For investigating reaction kinetics of CO₂ photoreduction in single gas phase, the thin-film flatbed with simple reactor configuration and simple mass transfer process is preferred because it is less affected by relatively complex mass transfer process than the slurry bed or packed bed [9]. For example, for the standardisation in testing conditions to make the assessment of process parameters, Olivo et al. [18] investigated the irradiance and reaction parameters of CO₂ photoreduction on production of CH₄ in two thin-film photoreactors. Previously, the first-order or pseudo first-order Langmuir-Hinshelwood model was applied for the reaction kinetics [10], while for the radiation model, the line source spherical emission was employed for describing the radiation field neglecting the attenuation along the *z*-direction [19]. However, the simplification of reaction kinetics and description of the radiation field may lose some details of the whole reaction process, e.g., nonlinear reaction process and reaction contribution by the thin film along the *z*-direction besides the surface along the *x*- and *y*-directions.

The purpose of this work is to understand the mechanism of CO₂ photoreduction using Langmuir theory and surface reaction. The novelty is that this work uniquely develops and combines a three-step intrinsic kinetic model that included adsorption, surface reactions and desorption, as well as a unique irradiation model that considered the depth of the thin film in combination of the Gaussian equation and the Beer-Lambert equation. Hence, the kinetic model, which was developed in this study, used CFD modeling as an effective tool to understand and differentiate flow behavior and surface reactions. This is used for the first time in modeling CO₂ photoreduction process. By using this unique approach, it is possible to improve the whole CO₂ photoreduction process as well as provide guidance for photoreactor design. This approach

also allowed to explore the dominant parameters influencing the CO₂ photoreduction and guide experimental studies.

2 Simulation of CO₂ photoreduction

2.1 CO₂ photoreduction in a thin-film reactor

In this work, the photoreactor dimensions and CO₂ photoreduction conditions for simulation originate from published work [11]. The schematic diagram of the photoreactor is shown in Fig. 1. The diameter and height of the reactor are 50 and 1 mm, respectively. The diameters of the gas inlet and outlet are 0.8 and 1.2 mm, respectively. The photocatalyst support mesh has dimensions of 25 mm × 40 mm. The thickness of the catalyst thin film is 0.2 mm. The gas mixture of Ar, CO₂ and water moisture (H₂O) enters the reactor at a flow rate of 0.35 mL·min⁻¹ and the product mixture of H₂, CO and CH₄ with unreacted gases flows out of the reactor into the gas chromatograph (GC). The whole reactor was placed on the hotplate and the temperature was controlled at 314.15 K. The intensity of the UV light (wavelength 365 nm) at the end of the optical fiber is 400 mW·cm⁻². The average UV light intensity on the surface of the photocatalyst film is 160 W·m⁻².

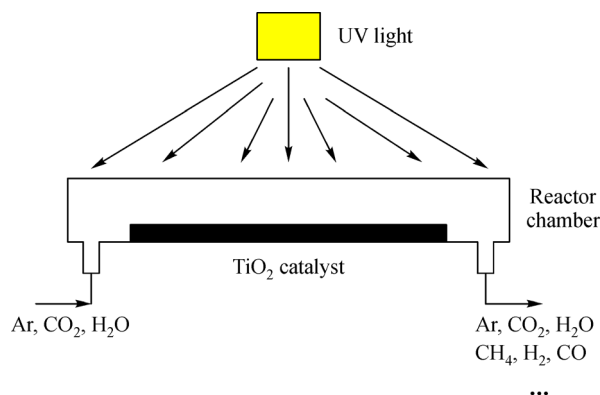


Fig. 1 Schematic diagram of the studied CO₂ photoreduction reactor.

Thompson et al. [9] pointed out that the partial pressures of both CO₂ and H₂O are likely to influence the reaction rate. Therefore, the experiments were divided into two groups: 1) CO₂ partial pressure from 25.72 to 98.38 kPa; 2) H₂O partial pressure from 2.66 to 6.64 kPa. The detailed experimental conditions are presented in Table 1.

2.2 CO₂ photoreduction mechanism

Kočí et al. [20] and Ji and Luo [21] studied the mechanism of CO₂ photoreduction to CH₄ on the anatase TiO₂ surface by the first-principles calculation on the thermodynamically

Table 1 Experimental conditions

Experiment No.	Experiment code ^{a)}	Photocatalyst loading/mg	CO ₂ partial pressure /kPa	Ar partial pressure /kPa	H ₂ O partial pressure /kPa	Flow rate /($\times 10^{-9}$ m ³ ·s ⁻¹)
1	PCO ₂ H	83.0	25.72	74.30	2.66	5.9883
2	PCO ₂ I	83.0	48.44	48.44	2.74	6.0030
3	PCO ₂ L	83.0	98.38	0	2.62	5.9883
4	PH ₂ OH	90.6	25.72	74.30	2.66	5.9886
5	PH ₂ OI	90.6	25.50	73.67	3.47	6.0367
6	PH ₂ OL	90.6	24.67	71.27	6.64	6.2367

a) H, I and L stand for relatively high, intermediate and low pressure, respectively, of Ar.

cally feasible formaldehyde (HCHO) pathway. They showed that CO₂ photoreduction will be more efficient when the formation of CO is preferred if CO instead of formic acid (HCOOH) during the reduction process. Thompson et al.'s work [11] showed that CO is one of dominant intermediate products, and thus, in this work we chose and treated the potential CO pathway as the main reaction route for CO₂ photoreduction to CH₄. To further simplify the reaction route, the intermediate products of HCHO and methanol (CH₃OH) are not considered in our simulation and CO directly generates CH₄.

2.3 Governing equations

In this work, the CO₂ photoreduction takes place in a one-phase gas flow reactor, where the flow is in the laminar regime ($Re_{in} < 0.1$). The photocatalyst thin film is treated as a surface with the size of 40 mm \times 25 mm. The assumptions employed for the photoreduction reactor include: 1) the gas flow is in the steady-state; 2) the gas is incompressible; 3) the gas density and viscosity are constant during the whole process and are obtained by the mixture mole ratio of Ar, CO₂ and H₂O. Because the generated quantity of CH₄, CO and H₂ with concentration around 10^{-4} mol·m⁻³ is much smaller than that of Ar, CO₂ and H₂O with concentration around 1–20 mol·m⁻³, we do not consider the change of gas density with the studied reactions; 4) the gas enters the reactor at the inlet with a uniform constant velocity distribution; 5) the reactor wall is adiabatic; 6) the heating caused by the UV lighting is negligible; 7) the photocatalyst is always active during the process and the deactivation of photocatalysts is not considered in this work; 8) the hole and electron generation and recombination activated by the UV lighting are very fast and do not influence the hole and electron trapping reactions; 9) the temperature distribution is uniform.

The governing equations are as follows:

(1) Mass equation

$$\rho \nabla \cdot (\mathbf{u}) = m_s, \quad (1)$$

where ρ is the density; \mathbf{u} is the velocity; m_s is the mass source.

(2) Momentum equation

$$\rho(\mathbf{u} \cdot \nabla) \mathbf{u} = \nabla \cdot [-p + \mu(\nabla \mathbf{u} + (\nabla \mathbf{u})^T)], \quad (2)$$

where p is the pressure; μ is the kinematic viscosity.

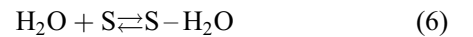
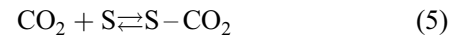
(3) Species equation

$$\nabla \cdot (-D_i \nabla c_i) + \mathbf{u} \cdot \nabla c_i = R_i, \quad (3)$$

where D_i is the diffusivity; c_i is the mole concentration; R_i is the reaction mass source.

2.4 Langmuir adsorption

The mass transfer between the bulk flow and photocatalyst surface is described by the Langmuir adsorption model. The gas adsorption and desorption are reversible and the adsorption of gas species on the surface is related to the gas partial pressure and adsorption sites (S). The adsorption steps are shown in the following reactions.



The adsorption rate is

$$r_{ad} = k_{ad} p_i [\text{S}] \quad (11)$$

where r_{ad} is the adsorption rate; k_{ad} is the adsorption rate constant; p_i is the partial pressure; $[\text{S}]$ is the bare site density. The desorption rate is

$$r_{de} = k_{de} [c_{ad}], \quad (12)$$

where r_{de} is the desorption rate; k_{de} is the desorption rate constant; $[c_{\text{ad}}]$ is the adsorbed concentration.

If the desorption is described by the Arrhenius model, the kinetic constant is

$$k_{\text{de}} = A_{\text{d}} e^{-\frac{E_{\text{d}}}{RT}}, \quad (13)$$

where A_{d} is the frequency factor; R is the gas constant. E_{d} is the heat of desorption [22].

$$E_{\text{d}} = -\Delta H_{\text{ad}} - \frac{1}{2}RT, \quad (14)$$

where ΔH_{ad} is the adsorption enthalpy. The adsorption equilibrium constant is

$$K_{\text{eq}} = \frac{k_{\text{ad}}}{k_{\text{de}}}, \quad (15)$$

where K_{eq} is the adsorption equilibrium constant.

2.5 UV lighting

In this work, the irradiation model neglects the absorption, scattering or emission of radiation by the gaseous media in the reactor, which follows the literature [19].

The UV light intensity distribution along the x , y -directions is described by the Gaussian distribution model. The light intensity distribution is

$$I(r) = I_{(0)} e^{-\frac{2r^2}{\omega_0^2}}, \quad (16)$$

where I is the light intensity; r is the radius and ω_0 is the beam radius.

The radiative transport equation (RTE, Eq. (17)) comprising the light absorption, extinction, and scattering is used to model the UV light intensity along the thin-film thickness. In this work, the UV light radiative intensity is dominated by scattering and extinction [23]:

$$\begin{aligned} \Omega \cdot \nabla I(\Omega) &= \kappa I_{\text{b}}(T) - \beta I(\Omega) \\ &+ \frac{\sigma_{\text{s}}}{4\pi} \int I(\Omega') \phi(\Omega', \Omega) d\Omega', \end{aligned} \quad (17)$$

where, $I(\Omega)$ is the radiative intensity at a given position following the Ω direction; κ , absorption coefficient; β , extinction coefficient; σ_{s} , scattering coefficient.

Finally, the UV light intensity distribution along the z -direction can be simply described by the Beer-Lambert model. The light intensity distribution is

$$I(z) = I_1 e^{-\mu_{\text{L}} z}, \quad (18)$$

where μ_{L} is the attenuation coefficient; z is the depth of lighting in the object.

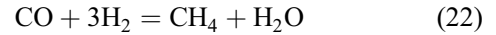
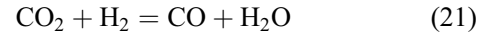
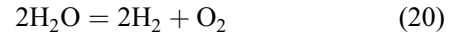
Due to the attenuation of light intensity, we divided the film into ten layers. To easily perform the simulation, the real three-dimensional photocatalyst thin film in this work

was considered as a XY plate surface to overcome the difficulty of meshing, but this causes the XY plate surface area is less than the real area of the thin film. As gas adsorption, reaction and desorption directly depend on the number of active sites on the surface, here we assume all the adsorption sites in the real thin film are distributed uniformly on the XY plate surface in the physical model. The light intensity for the surface reaction model is

$$\begin{aligned} I \cdot \frac{A_{\text{e}}}{A_{\text{t}}} &= I_{1.0} \cdot \frac{z_{1.0}}{z_{\text{t}}} + I_{0.9} \cdot \frac{z_{0.9}}{z_{\text{t}}} + I_{0.8} \cdot \frac{z_{0.8}}{z_{\text{t}}} + \dots \\ &+ I_{0.1} \cdot \frac{z_{0.1}}{z_{\text{t}}}. \end{aligned} \quad (19)$$

2.6 Surface reactions

From prior theoretical [21] and experimental investigations [11], CO is the preferred intermediate of CO_2 photoreduction on the P25 TiO_2 thin film. Therefore, we consider the CO_2 photoreduction mechanism described in Section 2.2 [21] as $\text{CO}_2 \rightarrow \text{CO} \rightarrow \text{HCHO} \rightarrow \text{CH}_3\text{OH} \rightarrow \text{CH}_4$ and simplification of the intermediate reactions between CO and CH_3OH as CO directly to generate CH_4 , where the surface reactions are shown as follow:



The reaction rate is

$$r_{\text{r}} = k_{\text{r}} I \frac{A_{\text{e}}}{A_{\text{t}}} [c_i]^m [c_j]^n, \quad (23)$$

where r_{r} is the reaction rate; k_{r} is the reaction rate constant; A_{e} is the effective lighting area; A_{t} is the total area of the photocatalyst; m , n is the order of the reaction. The reaction constant is

$$k_{\text{r}} = A_{\text{r}} e^{-\frac{E_{\text{a}}}{RT}}, \quad (24)$$

where A_{r} is the frequency factor; E_{a} is the activation energy.

2.7 Simulation method

The simulation was performed using COMSOL version 5.2a. The three modules, including laminar flow, transport of diluted species and general form boundary partial differential equations (PDE) were employed. The Newton-Raphson method is used for discretization of all the differential equations. For laminar flow, P2 (velocity) + P1 (pressure) is used. For species dilute transport and boundary, the quadratic method is used. The simulation

process has two consecutive steps: first, the fully coupled velocity, and pressure are solved; followed by the fully coupled species transport and surface reactions. For the nonlinear iterative method, the flexible generalized minimal residual method is used. The relative tolerance is 0.001. The factor in error estimate is 80. The scaling manual method is employed. The scale for the species in the bulk flow is 10^{-5} and the scale for the species in the surface is 10^{-12} . In this work, the CO₂ photoreduction process is considered to be steady-state, which is the same as described in other literatures [24,25], and thus, the simulation was solved by the stationary solver. In addition, modeling the deactivation is a separate issue as there are many unknown factors with respect to what the causes are such as catalyst deactivation and external conditions. For example, Thompson et al. [11] introduced a probability function to approximate the loss of active sites or deactivation.

2.8 Mesh

Figure 2 shows the physical model of the CO₂ photoreduction reactor and mesh in this work. Figure 2(a) shows the physical model as described in Section 2.1. The mesh 1, shown in Figs. 2(b–d), has 179856 grids with corner refinement, boundary layers and film surface refinement, which was automatically generated based on the user-controlled mesh setting in COMSOL and element sizes were calibrated for the physical principle of fluid dynamics. Mesh 2, shown in Fig. 2(e), comprises 288781 grids and was generated by using COMSOL predefined normal method for fluid dynamics. The

percentages of difference between these two meshes for the final CH₄ concentration, CO concentration and H₂ concentration are 0.0%, 3.0% and 4.3%, respectively. Therefore, mesh 1 with 179856 grids was used in this work.

2.9 Simulation conditions

The simulation conditions are described here. The site density is $3.6 \times 10^{-6} \text{ mol} \cdot \text{m}^{-2}$ or $2.31 \text{ sites} \cdot \text{nm}^{-2}$ [26]. The specific surface area of P25 TiO₂ is $53.31 \text{ m}^2 \cdot \text{g}^{-1}$ [11]. The diffusivity on the surface is $5 \times 10^{-8} \text{ m}^2 \cdot \text{s}^{-1}$ [27]. The temperature of the reactor is fixed at 314.15 K, which is the same as the temperature of the hotplate. Finally, the average concentration of the gas outlet is regarded as the species concentration determined by the GC. The average intensity on the surface of the photocatalyst is $160 \text{ W} \cdot \text{m}^{-2}$ [11], which was measured by using a fiber optic guide and an OmniCure R2000 radiometer. The physical properties of the gas species and properties of gas adsorption on the TiO₂ photocatalyst are shown in Table 2. The gas adsorption data were obtained from prior published work [22]. This is also the case for CO₂ and H₂O equilibrium constants [28] and the other equilibrium constants were estimated based on the literature [22,26–28] and matched with the experimental results under the conditions of PCO₂H.

A_r for reaction Eqs. (20), (21) and (22) is 6.1×10^{38} , $8.2 \times 10^{17} \text{ m}^4 \cdot \text{s}^{-1} \cdot \text{W}^{-1} \cdot \text{mol}^{-1}$ and $1.1 \times 10^{41} \text{ m}^8 \cdot \text{s}^{-1} \cdot \text{W}^{-1} \cdot \text{mol}^{-3}$, respectively. E_a for reaction Eqs. (20), (21) and (22) is 239.0, 67.54 and 42.5 kJ·mol⁻¹, respectively. The activation energy is estimated from the conversion of the

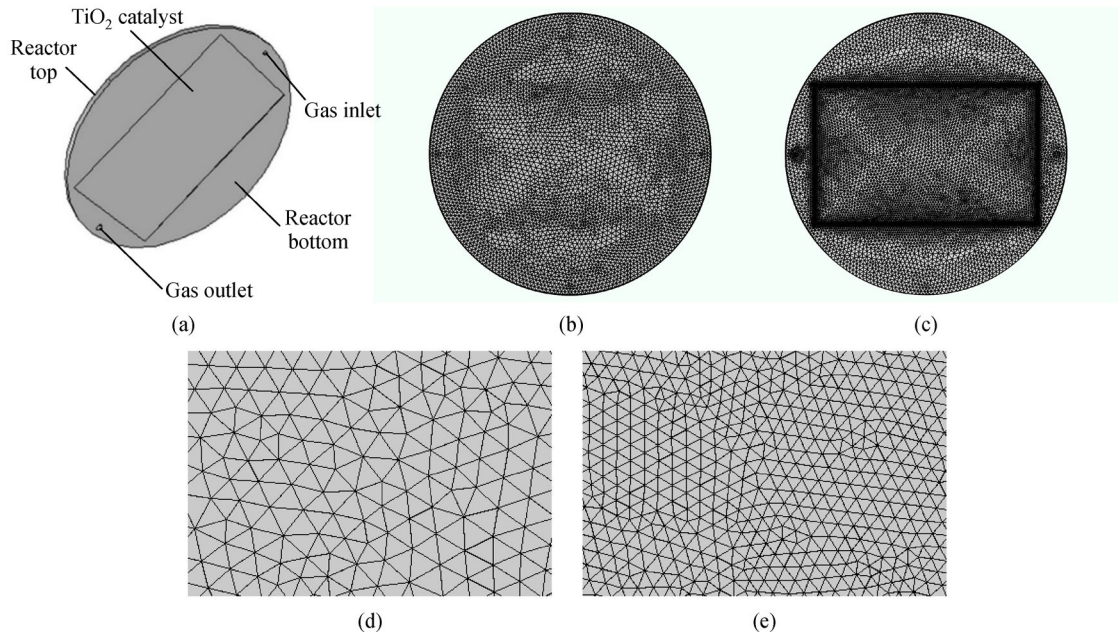


Fig. 2 Physical model and mesh: (a) physical model; (b) mesh 1 from top view; (c) mesh 1 from bottom view; (d) mesh 1 at the local area; (e) mesh 2 at the local area.

Table 2 Physical properties of gas species and properties of gas adsorption for the TiO₂ photocatalyst [22,28–30]

Gas	$D_f/(m^2 \cdot s^{-1})$	Adsorption		K_c/Bar^{-1}	$\mu/(\text{Pa} \cdot s)$	$\rho/(\text{kg} \cdot m^{-3})$
		A_d/s^{-1}	$-\Delta H_{ad}/(\text{kJ} \cdot \text{mol}^{-1})$			
Ar	1.89×10^{-5}	$10^{12.8}$	8.4	0.021	2.23×10^{-5}	1.78
CO ₂	1.60×10^{-5}	$10^{19.6}$	77.2	0.019	1.47×10^{-5}	1.98
H ₂ O	7.56×10^{-5}	$10^{14.6}$	83.7	8.070	2.55×10^{-4}	0.033
H ₂	7.56×10^{-5}	$10^{19.6}$	100.0	0.090		
O ₂	1.76×10^{-5}	$10^{13.8}$	16.4	0.020		
CO	2.08×10^{-5}	$10^{14.3}$	39.6	0.003		
CH ₄	2.10×10^{-5}	$10^{13.1}$	12.0	0.031		

potential energy level [21]. Because the frequency factors for the reaction rate constants are not known in advance, here they are assumed to the frequency factors which were obtained through simulation matching the experimental results under the condition of PCO2H.

3 Results and discussions

3.1 UV light distribution

The simulation of UV light distribution was performed with a two-dimensional RTE. The physical model and simulation results are shown in Fig. 3. Figure 3(a) shows the schematic diagram of physical model. The incident UV light with the intensity of $160 \text{ W} \cdot \text{m}^{-2}$ is irradiated on the top surface of the TiO₂ thin film. The thickness of the thin film is 0.2 mm. The simulation result is shown in Fig. 3(b). It is found that the light intensity on the top surface is ten times that of the incident light intensity due to light scattering on the surface. Moreover, the light intensity decreases steeply and approaches zero after 0.198 mm along the z -direction of the thin film. The effective thickness for UV lighting on thin film is 0.002 mm. Finally, the UV light intensity distribution can be written in the form of Beer-Lambert equation in Eq. (25).

$$I_{(z)} = 10.2957I_{\text{in}}e^{-2971440z}. \quad (25)$$

3.2 Velocity, pressure and concentration

In the simulation, we considered the path of $\text{CO}_2 \rightarrow \text{CO} \rightarrow \text{CH}_4$ as the dominant reaction route. Therefore, seven species, including Ar, CO, CO₂, H₂, O₂, CH₄ and H₂O, and three reactions, including reaction Eqs. (20), (21) and (22) (Section 2.6), are considered.

Figure 4 shows the typical gas flow and CO₂ photo-reduction process. The modeled gas velocity distribution in the reactor and gas pressure contour are shown in Figs. 4(a) and 4(b). The gas velocity is $1\text{--}10 \times 10^{-4} \text{ m} \cdot \text{s}^{-1}$ and the gas pressure is 0.007 Pa. The velocity distribution and pressure distribution are as expected. During the process, the CO₂ and H₂O concentrations in the gas flow are 9.85 and 1.02 $\text{mol} \cdot \text{m}^{-3}$, respectively. The CO₂ and H₂O concentrations on the film are 6.3×10^{-7} and $2.77 \times 10^{-5} \text{ mol} \cdot \text{m}^{-2}$, respectively. The typical product concentrations of CH₄ in the bulk flow and photocatalyst surface are up to $2.5 \times 10^{-4} \text{ mol} \cdot \text{m}^{-3}$ and $2.5 \times 10^{-11} \text{ mol} \cdot \text{m}^{-2}$, respectively, as shown in Figs. 4(c) and 4(d). The concentrations of CH₄ in the gas bulk and on the surface rise along the direction from gas inlet to gas outlet.

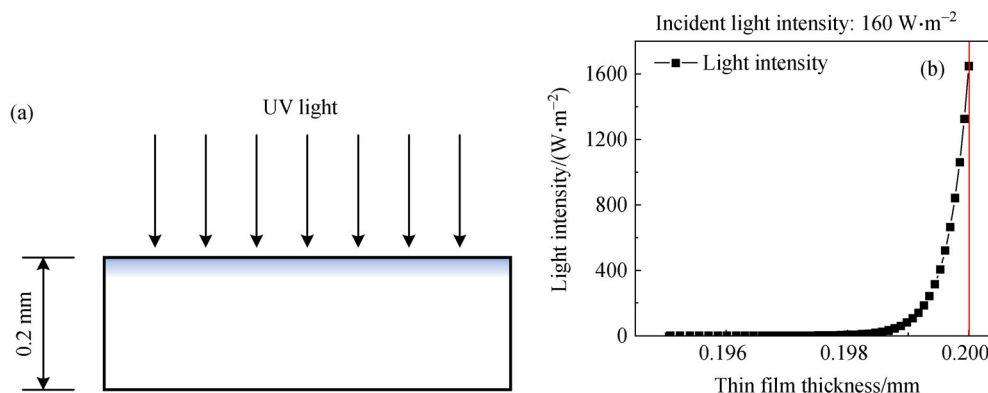


Fig. 3 UV light irradiation along the z -direction of the thin film: (a) physical model and (b) light intensity along the z -direction of the thin film.

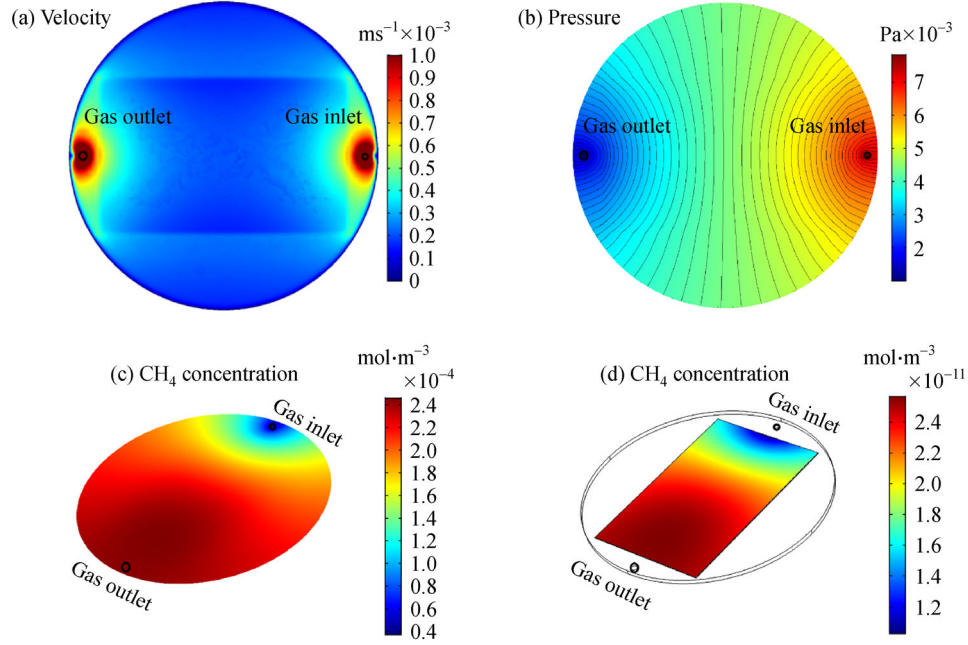


Fig. 4 Velocity, pressure and generated CH₄ distribution in the reactor. (a) Velocity from top view and (b) pressure contour; (c) CH₄ concentration in the bulk flow, which released from CH₄ on the catalyst surface; (d) CH₄ concentration on the photocatalyst surface, which generated from the photoreaction.

3.3 Validation of the models

The comparison between simulation and experimental results for CH₄, H₂ and CO concentrations is shown in Fig. 5. It can be seen that increasing CO₂ partial pressure from 25.72 to 98.38 kPa leads to the decrease of CH₄ concentration from 2.44×10^{-4} to 1.51×10^{-4} mol·m⁻³, as shown in Fig. 5(a). These match the experimental results for CH₄ concentration decreasing from 2.45×10^{-4} to 0.87×10^{-4} mol·m⁻³. The discrepancy of the simulation, which is the difference between simulation value and experimental value, δ_{sim} , is calculated using Eq. (26), which averages deviations between simulation and experimental values:

$$\delta_{\text{sim}} = \frac{\sum_{i=1}^{i=N} \frac{|d_{\text{sim}} - d_{\text{exp}}|}{d_{\text{exp}}}}{N}, \quad (26)$$

where d_{sim} is the simulation value; d_{exp} is the experimental value; N is the number of data pairs.

The discrepancy of CH₄ yield between simulation and experiment is around 30%. The predicted CH₄ concentration by simulation is in the reasonable range of the experimental data. Dilla et al. [24] also reported that increasing CO₂ concentration decreases the CH₄ yield due to the competition between O₂ and CO₂. Delavari et al. [31] reported that with increasing CO₂ partial pressure, there is an initial increase of CH₄ yield, followed by a

decrease. Thompson et al. [9] pointed out that there are two reasons for the decrease of CH₄ yield: 1) CO₂ dominates adsorption over H₂O to active sites; 2) an increase in repulsion between adsorbed CO₂ leading to larger surface diffusion activation energies causing reduced surface mobility. However, higher adsorption equilibrium constant for H₂O over CO₂ has also been reported [28]. The simulation work here has found that the CH₄ concentration has a linear proportional relationship with [CO] or of [H₂]³ (where 3 stands for the third order reaction for [H₂]). The decrease of CH₄ concentration is due to the decrease of the H₂ concentration in the experimental conditions, e.g., PCO2H, PCO2I and PCO2L. At the same time, the simulation studies also show that increasing CO₂ partial pressure from 25.72 to 98.38 kPa results in lower H₂ yields from 0.50×10^{-4} to 0.25×10^{-4} mol·m⁻³ (Fig. 5(b)). In contrast, the experimental results show that the H₂ yield decreases from 0.49×10^{-4} to 0.18×10^{-4} mol·m⁻³. The simulation discrepancy of H₂ yield is about 30%. The CO concentrations from experiments are in the range of 0.98×10^{-4} – 1.15×10^{-4} mol·m⁻³. The predicted CO concentration increases from 1.08×10^{-4} to 5.32×10^{-4} mol·m⁻³ (Fig. 5(c)). The simulated data predicted that CO concentration increases with higher CO₂ partial pressure under certain conditions, e.g., 98.38 kPa. This is different from the experimental data trend reporting that CO concentration decreases with increasing CO₂ partial pressure. However, the rule for predicted CO concentration matches the experiments by Lo et al. [32]. It demonstrates

that under some certain conditions, our model can still fully appropriately predict the trend with increasing CO_2 pressure.

The experimental studies (Fig. 5(d)) show that with increasing H_2O partial pressure, the CH_4 concentration is in the range of 1.92×10^{-4} – $2.82 \times 10^{-4} \text{ mol} \cdot \text{m}^{-3}$, while the simulation values show increasing CH_4 formation from 3.05×10^{-4} to $12.45 \times 10^{-4} \text{ mol} \cdot \text{m}^{-3}$. There is a big deviation between simulation and experiment for CH_4 yield at the higher H_2O partial pressure of 6.64 kPa that is discussed in the following section. In addition, the simulation data show that with increasing H_2O partial pressure from 2.66 to 6.64 kPa, the H_2 yield goes up from 0.48×10^{-4} to $2.53 \times 10^{-4} \text{ mol} \cdot \text{m}^{-3}$, as presented in

Fig. 5(e). The experimental results revealed that the production of H_2 rises from 0.49×10^{-4} to $1.27 \times 10^{-4} \text{ mol} \cdot \text{m}^{-3}$. The discrepancy of H_2 yield between simulation and experiment is about 30%. From adsorption and reaction kinetics standpoint, with increasing H_2O partial pressure, the H_2 and CH_4 are expected to increase, as demonstrated in the experiments by Khalilzadeh and Shariati [33]. The CO concentrations in the experiments are in the range of 1.08×10^{-4} – $1.30 \times 10^{-4} \text{ mol} \cdot \text{m}^{-3}$ and the predicted CO concentrations are in the range of 0.07×10^{-4} – $1.03 \times 10^{-4} \text{ mol} \cdot \text{m}^{-3}$ (Fig. 5(f)).

With the exception of the yield of CO in PCO2L and the yield of CH_4 in PH2OH, the total discrepancy of the simulation results compared to the experimental values is

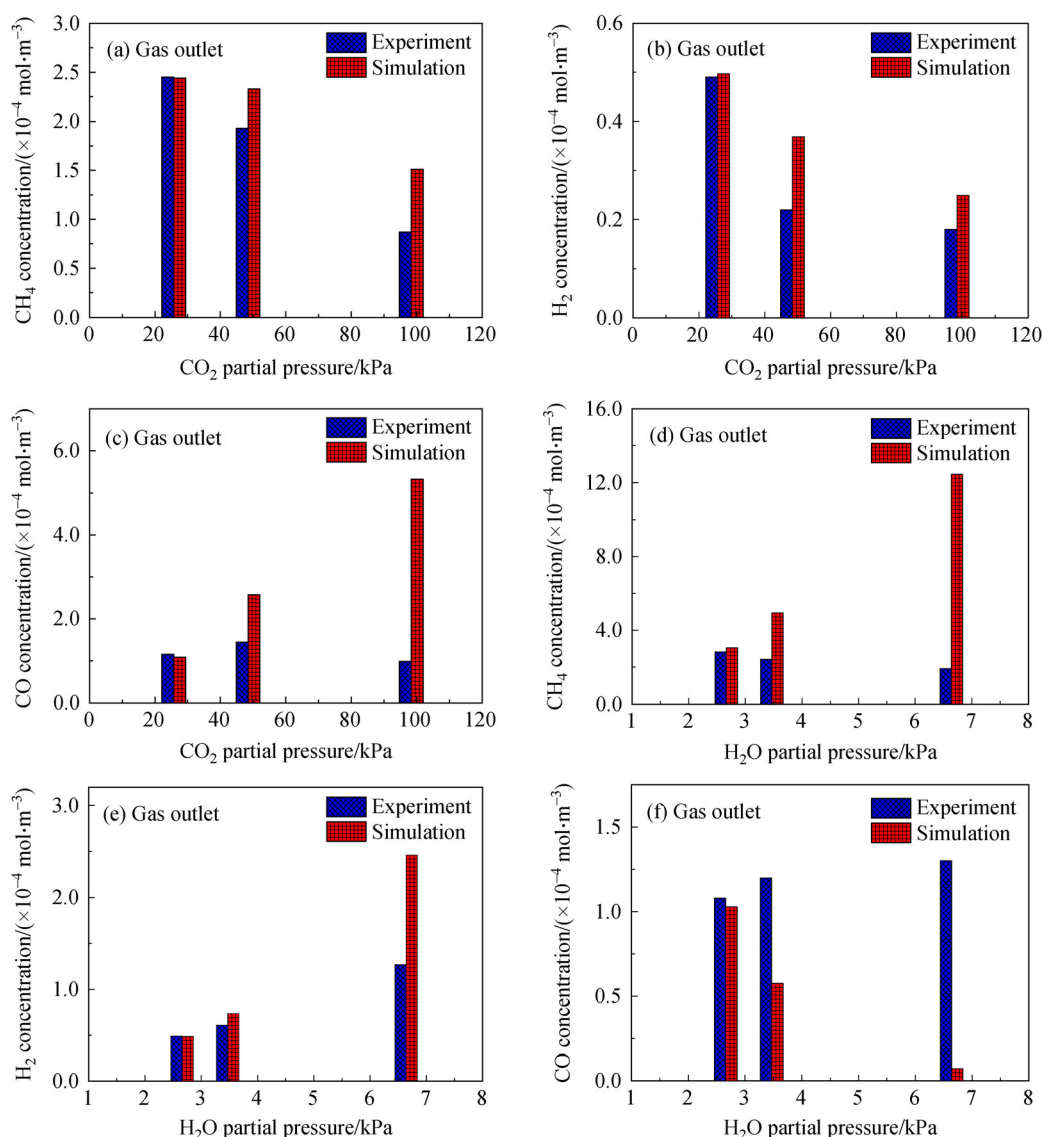


Fig. 5 Comparison between results from experiments and those based on simulation, concentration at the gas outlet under conditions of PCO2H, PCO2I and PCO2L: (a) CH_4 , (b) H_2 and (c) CO ; concentration at the gas outlet under conditions of PH2OH, PH2OI and PH2OL: (d) CH_4 , (e) H_2 and (f) CO .

within 30%–40%, that are 10%–20% higher than previous published simulation work [34]. These discrepancies might be due to the reasons as follows:

1) During CO₂ photoreduction, CH₄ is a key final product, but CO₂ also could be converted into other short-chain hydrocarbons, such as HCHO, HCOOH, CH₃OH, or even larger hydrocarbons, such as acetic acid (CH₃COOH) and acetaldehyde (CH₃CHO) [35]. Therefore, the activity and selectivity of reactions are key for production quantity of intermediate product CO and final product CH₄. The activity and selectivity of these reactions are determined by the thermodynamics and kinetics of these series of reactions [36]. From Figs. 5(c) and 5(f), it can be seen that when the CO₂ or H₂O partial pressure are higher than 48.44 or 3.47 kPa, respectively, the simulation result seems to contradict the experimental values. This may indicate that higher CO₂ and H₂O partial pressures can change the selectivity of CO₂ conversion to CH₄ and CO might be used to produce other products than CH₄. Kočí et al. [20] also demonstrated the CO₂ pressure influenced the CO₂ conversion to CH₄ in a gas-liquid-solid three-phase photoreactor. Unfortunately, Thompson's paper [11] did not report other potential products and only focused on CO and CH₄ as the main products. This may indicate that the combination of experiments and simulation could provide further understanding of the reaction mechanism of CO₂ photoreduction and also help to avoid the omission of reporting key experimental data. It also may be concluded that the current simulation and simplified reaction kinetics are only suitable for CO₂ and H₂O partial pressures below 48.44 and 3.47 kPa, respectively. Moreover, higher CO₂ and H₂O partial pressure decrease the selectivity of CO conversion to CH₄, and thus, may enhance the selectivity of CO₂ conversion to other products, such as CH₃COOH. Ola and Maroto-Valer [37] demonstrated that under certain conditions, the preferential product of CO₂ photoreduction is CH₃COOH or CH₃CHO, instead of CH₄. The effect of the reaction conditions on the selectivity of CO₂ photoreduction will be further investigated in our future work.

2) From the simulation, it can be seen that the discrepancy of CO or CH₄ between simulation results and experimental data are larger than that of H₂. During the CO₂ photoreduction process, O₂ is generated. H₂ can be oxidized by O₂/O₂[−] more easily than CO and CH₄. Thus, it seems that O₂/O₂[−] influences H₂ more than CO and CH₄. However, because CO and CH₄ are generated by reduction of CO₂ and CO through generated H₂ (Eqs. (21) and (22)), O₂/O₂[−] can greatly influence production of CO and CH₄ through free H₂ as well. For the CO generation reaction (Eq. (21)), the reaction rate is $k_r[\text{CO}] \times [\text{CO}_2] \times [\text{H}_2]$. For the CH₄ generation reaction (Eq. (22)), the reaction rate is $k_r[\text{CH}_4] \times [\text{CO}] \times [\text{H}_2]^3$. In addition, the reaction rate constant of CH₄ is much higher than that of CO and moreover, the reaction rate constant of CO is much higher than that of H₂ ($k_r[\text{CH}_4]$ (9.43×10^{33}) for Eq. (22) \gg $k_r[\text{CO}]$ (4.82×10^6) for Eq. (21) \gg $k_r[\text{H}_2]$ (0.11) for Eq. (20)

when $T = 314.15$ K). Therefore, this may affect the sensitivity of our predictions, resulting in higher CH₄ error than that of CO and much higher than that of H₂. From H₂ to CH₄, the error would gradually spread and expand. Therefore, the reaction is very sensitive to the frequency factor of the surface reactions, A_r . The 5% change of A_r may bring 50% change of CO, H₂ and CH₄ concentrations in the gas phase. This may be the main reason for the discrepancy from Eq. (26) in this work been higher than the general simulation. A_r may also change and sensitive to the environment, such as temperature. This implies that very small change of operating conditions, such as temperature, may bring significant changes in the gas production measured.

3) The photocatalytic activity is quite sensitive to oxygen on the surface of TiO₂ because O₂ seeks the oxygen vacancy defects of TiO₂, producing superoxide O₂[−] species as an oxidizing agent [38]. Thus, the superoxide species may reduce CO₂ photoreduction activity. Water splitting is key for the CO₂ photoreduction process and the generated O₂ needs to be quickly removed from the surface. To confirm the effect of the O₂ concentration on the surface, further experimental studies are needed.

A complete photocatalysis simulation requires the holistic knowledge on UV light propagation, semiconductor, fluid flow, diffusion, heat and mass transfer, adsorption and surface reactions. Currently, most models on CO₂ photoreductions are empirical or mechanistic models based mainly on adsorption and surface reactions [11,13]. Our work here advances current models by combining UV light propagation, flow dynamics, diffusion, and adsorption kinetics, as well as reaction kinetics to describe the CO₂ photoreduction process. In addition, the above discussion also indicates that combination of modeling and experiment is critical to reveal the mechanism of photocatalysis, and thus, provides a basis for further improving the efficiency of CO₂ photoreduction. The simulation results reported here were based on the available experimental data and well-known CO₂ photoreaction routes. With the enrichment of experimental data and development and improvement of new theoretical model formulas, the discrepancies are expected to be reduced further. Therefore, it is also possible to enhance further understanding of light-driven reactions.

3.4 Effect of CO and H₂ adsorption equilibrium constant

The gas adsorption equilibrium constant affects the concentration of produced gases on the surface and further influences the concentration in the bulk flow. The CO and H₂ intermediate gases are key for the whole CO₂ photoreduction process, so in this section, the effect of the CO and H₂ adsorption equilibrium constants has been investigated under the conditions of PCO2I and PH2OI. The simulation results are shown in Fig. 6.

Figures 6(a) and 6(b) show that with increasing CO

adsorption equilibrium constant from 0.0006 to 0.0106 Bar^{-1} , the CH_4 yield increases from 1.81×10^{-4} to $2.69 \times 10^{-4} \text{ mol} \cdot \text{m}^{-3}$ and the CO yield decreases from 4.36×10^{-4} to $1.32 \times 10^{-4} \text{ mol} \cdot \text{m}^{-3}$. Figures 6(d) and 6(e) show that with increasing H_2 adsorption equilibrium constant from 0.07 to 0.13 Bar^{-1} , the concentration of CH_4 increases from 4.80×10^{-4} to $5.10 \times 10^{-4} \text{ mol} \cdot \text{m}^{-3}$ and the H_2 concentration decreases from 0.90×10^{-4} to $0.53 \times 10^{-4} \text{ mol} \cdot \text{m}^{-3}$. These trends indicate that the CO and H_2 concentrations on the surface increase. The decrease of the CO or H_2 concentration in the bulk flow is caused by the increase of the CO or H_2 concentration on the photocatalyst surface from 0.77×10^{-12} to 4.15×10^{-12} and from 2.34×10^{-11} to $2.46 \times 10^{-11} \text{ mol} \cdot \text{m}^{-2}$, as shown in

Figs. 6(c) and 6(f) because of the higher CO or H_2 equilibrium constants.

The simulation results in Fig. 6 show that the adsorption equilibrium constant highly influences the yields of CH_4 , CO and H_2 . The increase of CO and H_2 adsorption equilibrium constants enhances the adsorption quantities of CO and H_2 on the photocatalyst surface.

3.5 Effect of adsorption site concentration

The number of bare sites plus the number of sites occupied by the gases is equal to the total number of adsorption sites on the photocatalyst surface. When the total number of adsorption sites is increased, it is possible for more gases to

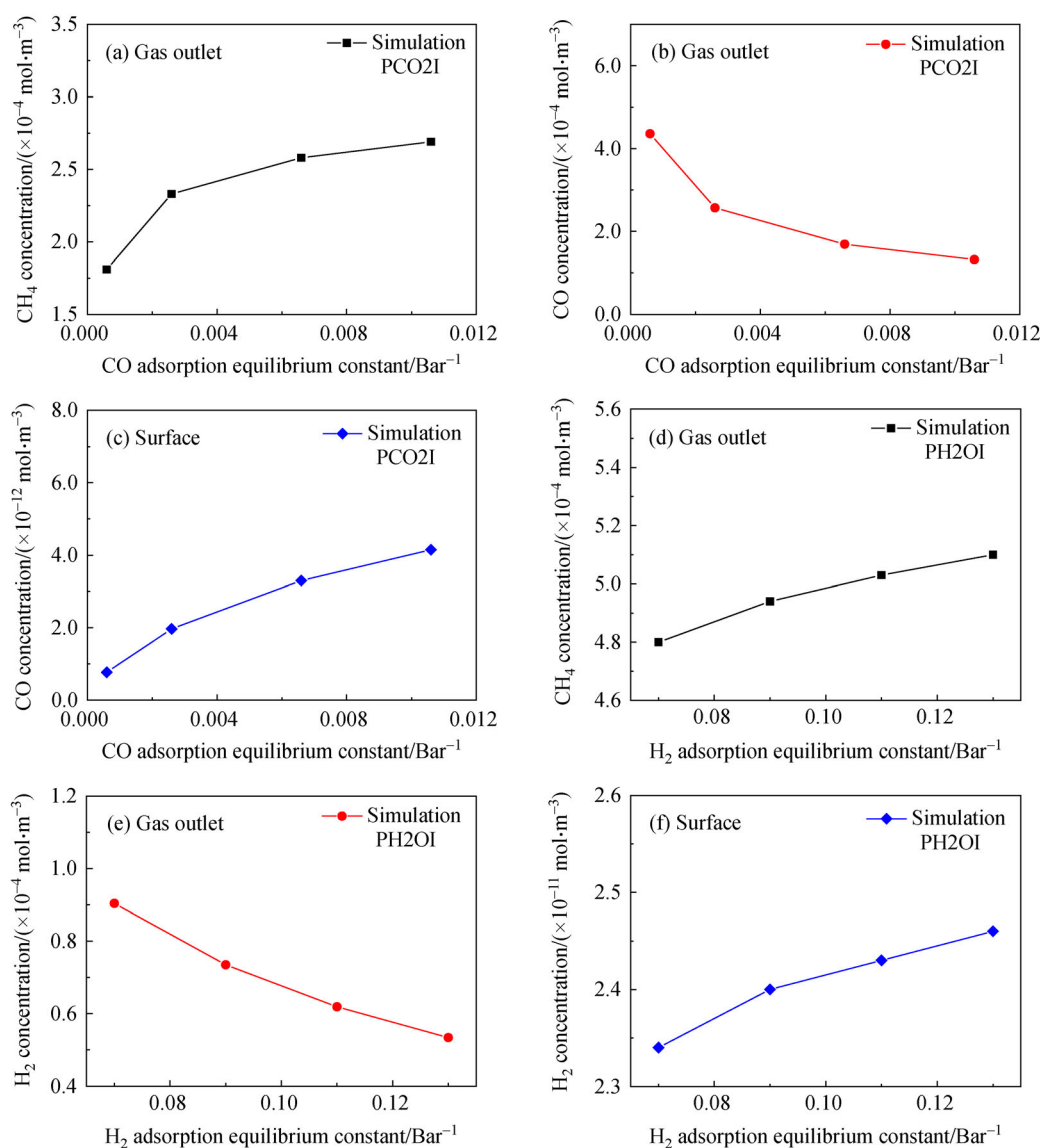


Fig. 6 Effect of CO and H_2 adsorption equilibrium constant. (a) CH_4 yield under PCO2I; (b) CO yield under PCO2I; (c) CO concentration on the photocatalyst surface under PCO2I; (d) CH_4 yield under PH2OI; (e) H_2 yield under PH2OI; (f) H_2 concentration on the photocatalyst surface under PH2OI.

be adsorbed on the photocatalyst surface. Therefore, the concentration of adsorption sites on the surface of the photocatalyst may strongly influence the concentration of produced gases on the surface as well as the concentration in the bulk flow. In this section, we explore the effect of adsorption site concentration on CO₂ photoreduction under the conditions of PCO2I and PH2OI and the simulation results are shown in Fig. 7.

Figures 7(a) and 7(c) show that with increasing adsorption sites concentration from 2.6×10^{-6} to $7.6 \times 10^{-6} \text{ mol} \cdot \text{m}^{-2}$, the CH₄ yield goes up from 0.84×10^{-4} to $24.51 \times 10^{-4} \text{ mol} \cdot \text{m}^{-3}$. Figures 7(b) and 7(d) show that with more adsorption sites, the concentrations of H₂ and CO in the bulk flow decline from 0.42×10^{-4} and 0.84×10^{-4} to 0.28×10^{-4} and $0.13 \times 10^{-4} \text{ mol} \cdot \text{m}^{-3}$, respectively. This indicates that more CO₂ and H₂ were adsorbed on the surface. Therefore, the adsorption site concentration has a great effect on the yield of CH₄, where more adsorption sites result in more gas adsorbed and higher CH₄ yields.

3.6 Effects of UV light intensity

The UV light irradiation plays a crucial role in photocatalytic processes and affects the photoreaction kinetics [9,32]. The reaction rate has a positive linear relationship with light intensity as shown in Eq. (23). This section examines the effect of UV light intensity on the CH₄ yield. The simulation results based on PCO2H are shown in Fig. 8.

Figure 8(a) shows the yields of CH₄, CO and H₂ and at the gas outlet with increasing UV light intensity. Figures 8(b–d) show the adsorption concentration of CH₄, CO and H₂ on the surface of the photocatalyst thin film. Figures 8(a), 8(b) and 8(c) indicate that when the average UV light intensity on the surface increases from 40 to $320 \text{ W} \cdot \text{m}^{-2}$, the CH₄ yield at the gas outlet and CH₄ concentration on the surface go up from $0.27 \times 10^{-4} \text{ mol} \cdot \text{m}^{-3}$ and $0.24 \times 10^{-11} \text{ mol} \cdot \text{m}^{-2}$ to $5.48 \times 10^{-4} \text{ mol} \cdot \text{m}^{-3}$ and $4.97 \times 10^{-11} \text{ mol} \cdot \text{m}^{-2}$, respectively. Concurrently, the CO yield at the gas outlet and CO concentration on the surface increase from $0.56 \times 10^{-4} \text{ mol} \cdot \text{m}^{-3}$ and $0.43 \times 10^{-12} \text{ mol} \cdot \text{m}^{-2}$ to $1.33 \times 10^{-4} \text{ mol} \cdot \text{m}^{-3}$ and $1.05 \times 10^{-12} \text{ mol} \cdot \text{m}^{-2}$, respectively. However, the production of H₂ is influenced by the UV light intensity limitedly. The H₂ concentrations at the gas outlet and surface are in the range of 0.47×10^{-4} – $0.50 \times 10^{-4} \text{ mol} \cdot \text{m}^{-3}$ and 1.44×10^{-11} – $1.56 \times 10^{-11} \text{ mol} \cdot \text{m}^{-2}$, as shown in Figs. 8(a) and 8(d). These results illuminate that the light intensity affects the production of CO higher than that of H₂.

3.7 Effect of temperature

The reactor temperature obviously affects the gas adsorption and reactions, and the effect of temperature was discussed in the literature [9]. Several researchers demonstrated that the higher temperature could promote trapping reactions and activity of CO₂ photoreduction [39]. In this section, the effect of different temperatures on CO₂

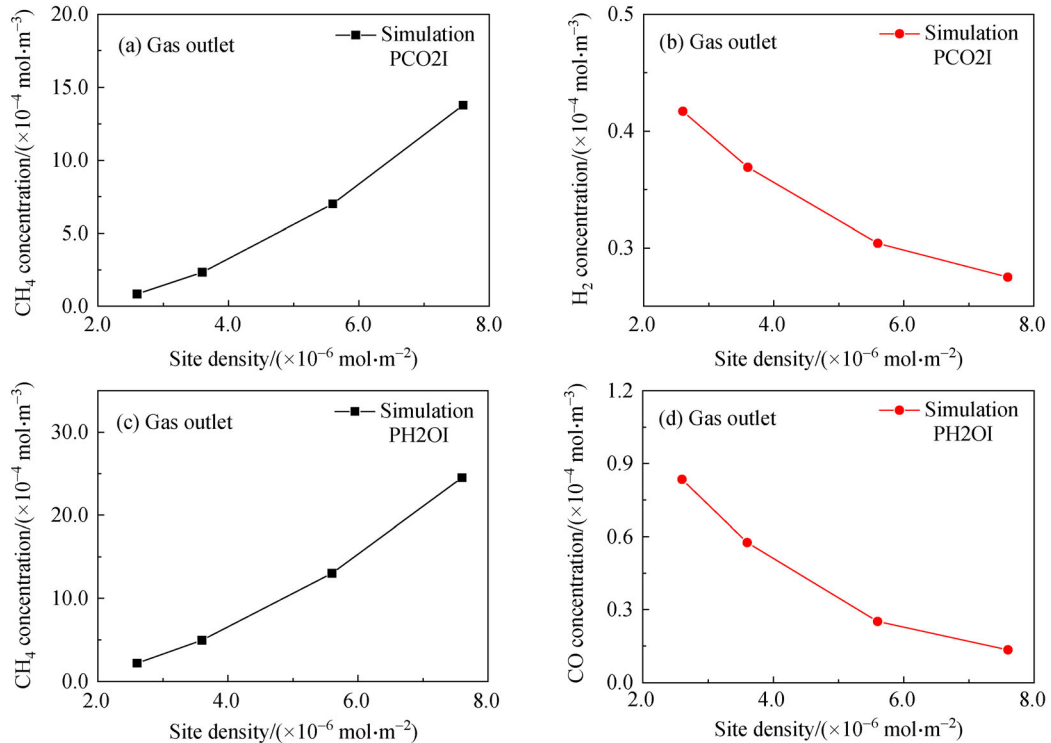


Fig. 7 Effect of adsorption site concentration. (a) CH₄ yield under PCO2I; (b) H₂ yield under PCO2I; (c) CH₄ yield under PH2OI; (d) CO yield under PH2OI.

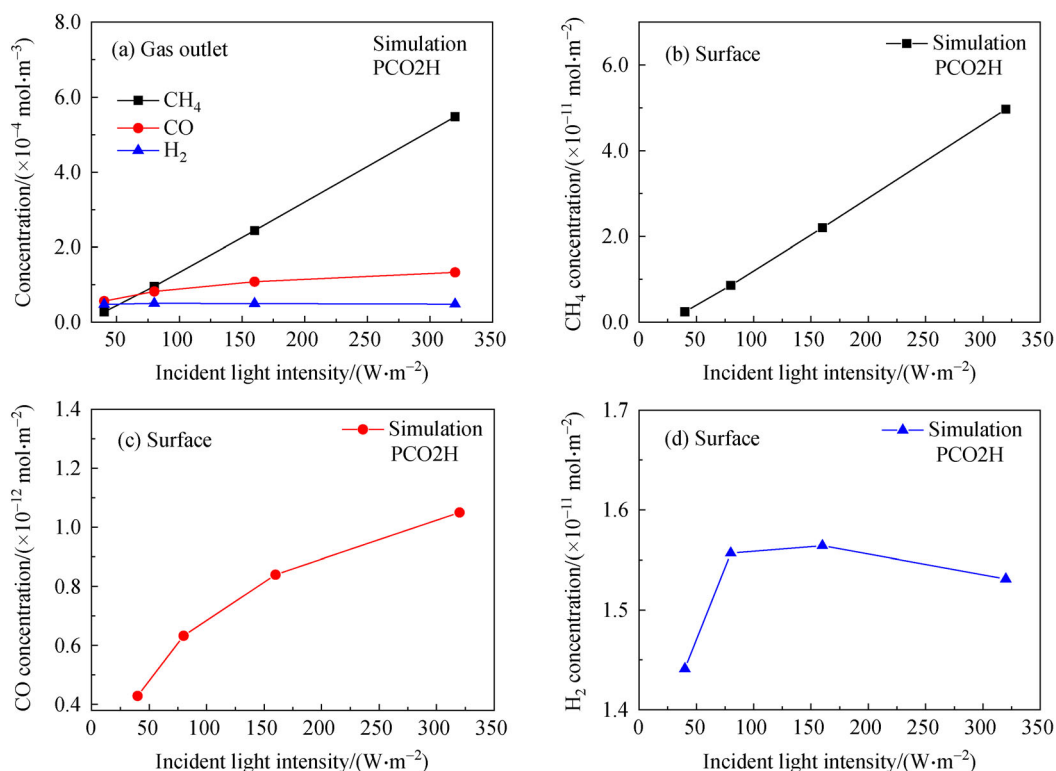


Fig. 8 Effect of increasing UV light intensity under PCO2H. (a) CH₄, CO, and H₂ yields at the gas outlet; (b) CH₄ concentration on the photocatalyst surface; (c) CO concentration on the photocatalyst surface; (d) H₂ concentration on the photocatalyst surface.

photoreduction was simulated using the validated models. In the simulation, the adsorption equilibrium constant is assumed to be constant in the temperature range of 309.15 K to 324.15 K. The simulation results based on PCO2H are shown in Fig. 9.

Figure 9(a) shows the yields of CH₄, CO, and H₂ at the gas outlet with increasing temperature. Figures 9(b–d) show the adsorption concentration of CH₄, CO and H₂ on the surface of the photocatalyst thin film with increasing temperature. As the temperature rises from 309.15 K to 324.15 K, the yields of CH₄ and H₂ increase from 0.27×10^{-4} and 0.25×10^{-4} to 49.24×10^{-4} and $3.25 \times 10^{-4} \text{ mol}\cdot\text{m}^{-3}$, respectively, and the concentrations of CH₄ and H₂ on the photocatalyst surface increase from 0.02×10^{-10} and 0.83×10^{-11} to 4.62×10^{-10} and $9.84 \times 10^{-11} \text{ mol}\cdot\text{m}^{-2}$, respectively. The yield of CO is in the range of 0.04×10^{-4} – $1.08 \times 10^{-4} \text{ mol}\cdot\text{m}^{-3}$. The concentration of CO on the photocatalyst surface is in the range of 0.44×10^{-13} – $8.40 \times 10^{-13} \text{ mol}\cdot\text{m}^{-2}$. It seems that the yield of H₂ is influenced by the temperature higher than the yield of CO.

CO₂ photoreduction process has two reaction steps, resulting in a wide range of possible potential products. Generally, the reaction steps include electron and carrier trapping reactions and radical propagation reactions. The UV light radiation with tuning wavelength may influence the selectivity of trapping reactions by energy level for driving force to overcome the reaction energy barrier. Tan et al. [40] demonstrated highly selective photoreduction of

CO₂ to generate CH₄ under irradiation above 600 nm. On the other hand, selectivity toward a given final product is mainly determined by the thermodynamic and kinetic reaction parameters of the CO₂ conversion reactions [36]. The issue of reaction selectivity can also be considered on the radical propagation reactions. Although Kočí et al. [20] indicated that CO₂ photoreduction was not sensitive significantly to small temperature change within 10 K, Kohno et al. [41] and Anpo [35] demonstrated high temperature resulted in change of reaction selectivity. Therefore, temperature affects the reaction selectivity. As a follow-up to the work reported here, the effect of UV light intensity and temperature on selectivity of intermediation reactions and products will be investigated.

In summary, it can be seen from the simulation studies that when using stronger light intensity and higher temperature, more CH₄ is produced. The tendency of gas product yields by this simulation with different UV light intensities and temperatures is in agreement with published work [32]. This conclusion gives a valuable guidance of adsorption kinetics and reaction kinetics for photoreactor and CO₂ photoreduction process design.

4 Conclusions

In this work, the CO₂ photoreduction process was simulated based on an intrinsic kinetic model by COMSOL

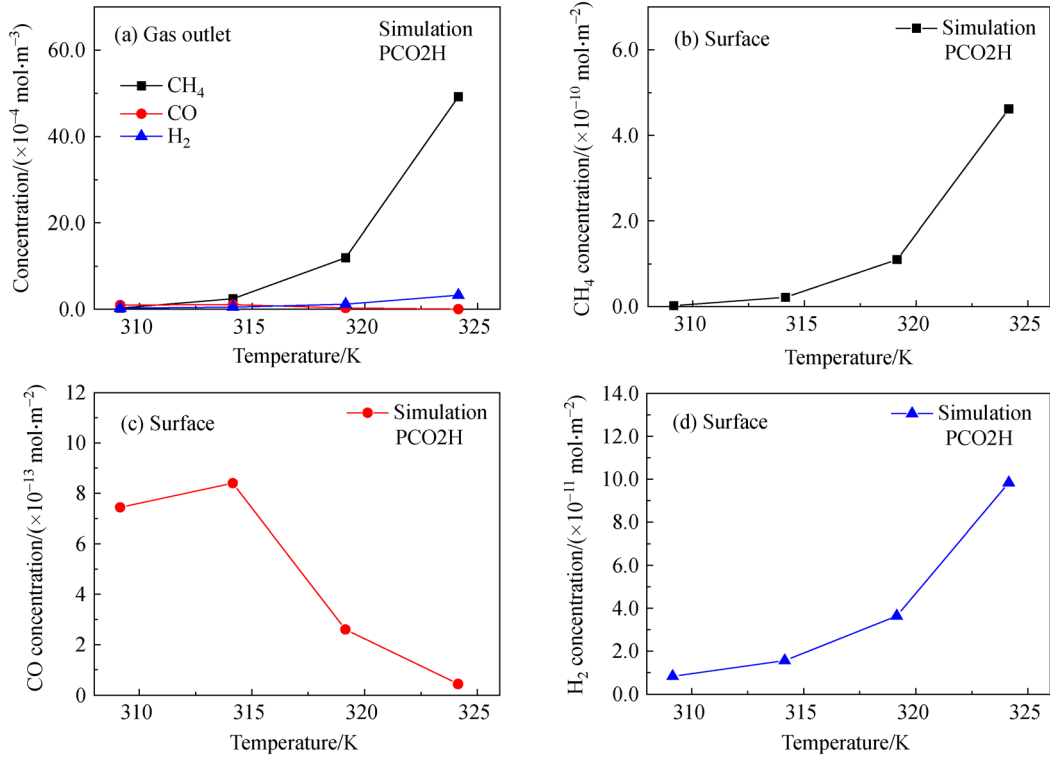


Fig. 9 Effect of increasing temperature under PCO₂H. (a) CH₄, CO and H₂ yields at the gas outlet; (b) CH₄ concentration on the photocatalyst surface; (c) CO concentration on the photocatalyst surface; (d) H₂ concentration on the photocatalyst surface.

version 5.2a including three modules: laminar flow module, species dilute transportation module and general form boundary PDE module. The mechanism of CO₂ photoreduction process is the reaction potential path: CO₂ → CO → HCHO → CH₃OH → CH₄. In our work, the intrinsic kinetic model comprises two parts: Langmuir adsorption/desorption and surface reactions. The novelty of this work is the combination of the intrinsic kinetic model with the CFD model to investigate the CO₂ photoreduction on the TiO₂ thin film. The simulation results are compared with the experimental results, and it was demonstrated that the simulation results are in the reasonable range of the experiments at the low CO₂ and H₂O partial pressure. The simulation shows that with increasing CO₂ partial pressure, the CH₄ and H₂ yields decrease and CO yield increases; while with increasing H₂O partial pressure, the CH₄ and H₂ yields increase and CO decreases. Some key factors such as adsorption, temperature and UV lighting have also been investigated in this work. The adsorption sites and equilibrium constant, temperature and UV lighting affect the surface concentration, and therefore, influences the yields of CH₄, CO and H₂.

From the analysis of the operating parameters above, it can be concluded that gas adsorption on the photocatalyst surface is one of the crucial steps for improving the CH₄ yield in the CO₂ photoreduction process. Water splitting

generates H₂ and most of surface reactions depend on H₂ or H⁺ on the photocatalyst surface. The separation of water splitting and CO₂ photoreduction by a proton exchange membrane could improve CO₂ conversion efficiency [15]. Therefore, the novel twin photoreactor [15], photoelectrocatalytic process [42,43] and thin-film reactor with modified photocatalysts [44] might be promising reactor designs for CO₂ photoreduction.

Nomenclatures

A_d	frequency factor for gas desorption (s ⁻¹)
A_e	effective area for UV lighting (m ²)
A_r	frequency factor for reaction (m ² ·s ⁻¹ ·mol ⁻¹ or m ⁶ ·s ⁻¹ ·mol ⁻³)
A_t	total area of the photocatalyst (m ²)
c_i	mole concentration of i species (mol·m ⁻³ (bulk) or mol·m ⁻² (surface))
$[c_{ad}]$	gas concentration adsorbed on the surface (mol·m ⁻²)
C_p	heat capacity (J·kg ⁻¹ ·K ⁻¹)
d_{exp}	experimental value (mol·m ⁻³)
d_{sim}	simulation value (mol·m ⁻³)
D_i	gas diffusivity of the i species (m ² ·s ⁻¹)
E_a	activation energy for reaction (kJ·mol ⁻¹)
E_d	activation energy for gas desorption (kJ·mol ⁻¹)

ΔH_{ad}	adsorption enthalpy ($\text{kJ} \cdot \text{mol}^{-1}$)
ΔH_{r}	reaction heat ($\text{kJ} \cdot \text{mol}^{-1}$)
I	light intensity ($\text{W} \cdot \text{m}^{-2}$)
$I(\Omega)$	radiative intensity at a given position following the Ω direction ($\text{W} \cdot \text{m}^{-2}$)
I_{in}	intensity of incident UV light ($\text{W} \cdot \text{m}^{-2}$)
k	thermal conductivity ($\text{W} \cdot \text{m}^{-1} \cdot \text{K}^{-1}$)
k_{r}	reaction constant ($\text{m}^2 \cdot \text{s}^{-1} \cdot \text{mol}^{-1}$ or $\text{m}^6 \cdot \text{s}^{-1} \cdot \text{mol}^{-3}$)
k_{ad}	adsorption constant ($\text{m} \cdot \text{s} \cdot \text{kg}^{-1}$)
k_{de}	desorption constant (s^{-1})
K	adsorption equilibrium constant (Bar^{-1})
r_{r}	reaction rate ($\text{mol} \cdot \text{m}^{-2} \cdot \text{s}^{-1}$)
r_{ad}	adsorption rate ($\text{mol} \cdot \text{m}^{-2} \cdot \text{s}^{-1}$)
r_{de}	desorption rate ($\text{mol} \cdot \text{m}^{-2} \cdot \text{s}^{-1}$)
p	gas partial pressure (Pa or Bar)
m	order for the reaction (–)
m_{s}	mass source ($\text{kg} \cdot \text{m}^{-3} \cdot \text{s}^{-1}$)
n	order for the reaction (–)
N	number of data (–)
r	radius (m)
R	gas constant, $8.314 \text{ (J}^{-1} \cdot \text{K}^{-1} \cdot \text{mol}^{-1})$
$[S]$	bare site concentration on the surface ($\text{mol} \cdot \text{m}^{-1}$)
t	time (s)
T	temperature (K)
u	velocity ($\text{m} \cdot \text{s}^{-1}$)
z	depth (m)

Greek symbols

β	extinction coefficient (m^{-1})
δ_{sim}	simulation discrepancy (–)
κ	absorption coefficient (m^{-1})
μ	dynamic viscosity (Pa·s)
μ_{L}	attenuation of the UV light (m^{-1})
ρ	density ($\text{kg} \cdot \text{m}^{-3}$)
σ_{s}	scattering coefficient (m^{-1})
ω_0	radius of light beam (m)

Subscripts

i, j gas species.

Acknowledgements The authors thank the financial support provided by the Engineering and Physical Sciences Research Council (Grant No. EP/K021796/1), the Research Centre for Carbon Solutions and the James Watt Scholarship Programme at Heriot-Watt University. We are also grateful for the support provided by the Buchan Chair in Sustainable Energy Engineering.

Open Access This article is licensed under a Creative Commons Attribution 4.0 International License, which permits use, sharing, adaptation, distribution and reproduction in any medium or format, as long as you give appropriate credit to the original author(s) and the source, provide a link to the Creative Commons licence, and indicate if changes were made. The images or other third party material in this article are included in the article's Creative Commons licence, unless indicated otherwise in a credit line to the material. If material is not included in the article's Creative Commons licence and your intended use is not permitted by statutory regulation or exceeds the permitted use, you will need to obtain permission directly from the copyright holder. To view a copy of this licence, visit <http://creativecommons.org/licenses/by/4.0/>.

References

- Lu X, Xie P, Ingham D B, Ma L, Pourkashanian M. Modelling of CO_2 absorption in a rotating packed bed using an Eulerian porous media approach. *Chemical Engineering Science*, 2019, 199: 302–318
- Izumi Y. Recent advances in the photocatalytic conversion of carbon dioxide to fuels with water and/or hydrogen using solar energy and beyond. *Coordination Chemistry Reviews*, 2013, 257(1): 171–186
- Tan L, Peter K, Ren J, Du B, Hao X, Zhao Y, Song Y. Photocatalytic syngas synthesis from CO_2 and H_2O using ultrafine CeO_2 -decorated layered double hydroxide nanosheets under visible-light up to 600 nm. *Frontiers of Chemical Science and Engineering*, 2021, 15(1): 99–108
- Song G, Wu X, Xin F, Yin X. ZnFe_2O_4 deposited on BiOCl with exposed (001) and (010) facets for photocatalytic reduction of CO_2 in cyclohexanol. *Frontiers of Chemical Science and Engineering*, 2017, 11(2): 197–204
- Hafez A M, Zedan A F, AlQaradawi S Y, Salem N M, Allam N K. Computational study on oxynitride perovskites for CO_2 photo-reduction. *Energy Conversion and Management*, 2016, 122: 207–214
- Schneider J, Matsuoka M, Takeuchi M, Zhang J, Horiuchi Y, Anpo M, Bahnemann D W. Understanding TiO_2 photocatalysis: mechanisms and materials. *Chemical Reviews*, 2014, 114(19): 9919–9986
- Qian R, Zong H, Schneider J, Zhou G, Zhao T, Li Y, Yang J, Bahnemann D W, Pan J H. Charge carrier trapping, recombination and transfer during TiO_2 photocatalysis: an overview. *Catalysis Today*, 2019, 335: 78–90
- Vorontsov A V, Valdes H, Smiriotis P G, Paz Y. Recent advancements in the understanding of the surface chemistry in TiO_2 photocatalysis. *Surfaces*, 2020, 3(1): 72–92
- Thompson W A, Fernandez E S, Maroto-Valer M M. Review and analysis of CO_2 photoreduction kinetics. *ACS Sustainable Chemistry & Engineering*, 2020, 8(12): 4677–4692
- Tahir M, Amin N S. Photocatalytic CO_2 reduction and kinetic study over In/TiO_2 nanoparticles supported microchannel monolith photoreactor. *Applied Catalysis A, General*, 2013, 467: 483–496
- Thompson W A, Fernandez E S, Maroto-Valer M M. Probability Langmuir-Hinshelwood based CO_2 photoreduction kinetic models. *Chemical Engineering Journal*, 2020, 384: 123356
- Marczewski A W. Analysis of kinetic Langmuir model. Part I: integrated Langmuir equation (IKL): a new complete analytical solution of the Langmuir rate equation. *Langmuir*, 2010, 26(19): 15229–15238
- Bloh J Z. A holistic approach to model the kinetics of photocatalytic reactions. *Frontiers in Chemistry*, 2019, 7: 128
- Li H, Yi F, Li X, Gao X. Numerical modelling of mass transfer processes coupling with reaction for the design of the ozone oxidation treatment of wastewater. *Frontiers of Chemical Science and Engineering*, 2021, 15(3): 602–614
- Chu F, Chen S, Li H, Yang L, Ola O, Maroto-Valer M M, Du X, Yang Y. Modeling photocatalytic conversion of carbon dioxide in bubbling twin reactor. *Energy Conversion and Management*, 2017,

- 149: 514–525
16. Chen H, Chu F, Yang L, Ola O, Du X, Yang Y. Enhanced photocatalytic reduction of carbon dioxide in optical fibre monolith reactor with transparent glass balls. *Applied Energy*, 2018, 230: 1403–1413
 17. Verbruggen S W, Lenaerts S, Denys S. Analytic versus CFD approach for kinetic modelling of gas phase photocatalysis. *Chemical Engineering Journal*, 2015, 262: 1–8
 18. Olivo A, Thompson W A, Bay E R B, Ghedini E, Menegazzo F, Maroto-Valer M, Signoreto M. Investigation of process parameters assessment via design of experiments for CO₂ photoreduction in two photoreactors. *Journal of CO₂ Utilization*, 2020, 36: 25–32
 19. Wang X, Tan X, Yu T. Kinetic study of ozone photocatalytic decomposition using a thin film of TiO₂ coated on a glass plate and the CFD modelling approach. *Industrial & Engineering Chemistry Research*, 2014, 53(19): 7902–7909
 20. Kočí K, Obalová L, Šolcová L. Kinetic study of photocatalytic reduction of CO₂ over TiO₂. *Chemical & Process Engineering*, 2010, 31: 395–407
 21. Ji Y, Luo Y. Theoretical study on the mechanism of photoreduction of CO₂ to CH₄ on the anatase TiO₂(101) surface. *ACS Catalysis*, 2016, 6(3): 2018–2025
 22. Campbell C T, Sellers J R V. Enthalpies and entropies of adsorption on well-defined oxide surfaces: experimental measurements. *Chemical Reviews*, 2013, 113(6): 4106–4135
 23. Meng X, Yun N, Zhang Z. Recent advances in computational photocatalysis: a review. *Canadian Journal of Chemical Engineering*, 2019, 97(7): 1982–1998
 24. Dilla M, Schlögl R, Strunk J. Photocatalytic CO₂ reduction under continuous flow high-purity conditions: quantitative evaluation of CH₄ formation in the steady-state. *ChemCatChem*, 2017, 9(4): 696–704
 25. Tseng I, Chang W, Wu J C S. Photoreduction of CO₂ using sol-gel derived titania and titania-supported copper catalysts. *Applied Catalysis B: Environmental*, 2002, 37(1): 34–48
 26. Giammar D E, Maus C J, Xie L. Effects of particle size and crystalline phase on lead adsorption to titanium dioxide nanoparticles. *Environmental Engineering Science*, 2007, 24(1): 85–95
 27. Mao W, Wilde M, Ogura S, Chen J, Fukutani K, Matsuzaki H, Terai T. Hydrogen-accelerated phase transition and diffusion in TiO₂ thin films. *Journal of Physical Chemistry C*, 2018, 122(40): 23026–23033
 28. Tan L L, Ong W J, Chai S P, Mohamed A R. Photocatalytic reduction of CO₂ with H₂O over graphene oxide-supported oxygen-rich TiO₂ hybrid photocatalyst under visible light irradiation: process and kinetic studies. *Chemical Engineering Journal*, 2017, 308: 248–255
 29. Lopes F V S, Grande C A, Ribeiro A M, Loureiro J M, Evaggelos O, Nikolakis V, Rodrigues A E. Adsorption of H₂, CO₂, CH₄, CO, N₂ and H₂O in activated carbon and zeolite for hydrogen production. *Separation Science and Technology*, 2009, 44(5): 1045–1073
 30. Bazan R E, Bastos-Neto M, Moeller A, Dreisbach F, Staudt R. Adsorption equilibria of O₂, Ar, Kr, and Xe on activated carbon and zeolites: single component and mixture data. *Adsorption*, 2011, 17(2): 371–383
 31. Delavari S, Amin N A S. Photocatalytic conversion of CO₂ and CH₄ over immobilized titanic nanoparticles coated on mesh optimization and kinetic study. *Applied Energy*, 2016, 162: 1171–1185
 32. Lo C C, Hung C H, Yuan C S, Hung Y L. Parameter effects and reaction pathways of photoreduction of CO₂ over TiO₂/SO₄²⁻ photocatalyst. *Chinese Journal of Catalysis*, 2007, 28(6): 528–534
 33. Khalilzadeh A, Shariati A. Photoreduction of CO₂ over heterogeneous modified TiO₂ nanoparticles under visible light irradiation: synthesis, process and kinetic study. *Solar Energy*, 2018, 164: 251–261
 34. Sebastia-Saez D, Gu S, Ranganathan P, Papadikis K. Meso-scale CFD study of the pressure drop, liquid hold-up, interfacial area and mass transfer in structured packing materials. *International Journal of Greenhouse Gas Control*, 2015, 42: 388–399
 35. Anpo M. Photocatalytic reduction of CO₂ with H₂O on highly dispersed Ti-oxide catalysts as a model of artificial photosynthesis. *Journal of CO₂ Utilization*, 2013, 1: 8–17
 36. Yin W, Wen B, Ge Q, Li X, Teobaldi G, Liu L. Activity and selectivity of CO₂ photoreduction on catalytic materials. *Dalton Transactions (Cambridge, England)*, 2020, 49(37): 12918–12928
 37. Ola O, Maroto-Valer M M. Transition metal oxide based TiO₂ nanoparticles for visible light induced CO₂ photoreduction. *Applied Catalysis A, General*, 2015, 502: 114–121
 38. Thompson T L, Yates J T Jr. TiO₂-based photocatalysis: surface defects, oxygen and charge transfer. *Topics in Catalysis*, 2005, 35(3–4): 197–210
 39. Li D, Huang Y, Li S, Wang C, Li Y, Zhang X, Liu Y. Thermal coupled photoconductivity as a tool to understand the photothermal catalytic reduction of CO₂. *Chinese Journal of Catalysis*, 2020, 41(1): 154–160
 40. Tan L, Xu S, Wang Z, Xu Y, Wang X, Hao X, Bai S, Ning C, Wang Y, Zhang W, et al. Highly selective photoreduction of CO₂ with suppressing H₂ evolution over monolayered double hydroxide under irradiation above 600 nm. *Angewandte Chemie*, 2019, 131(34): 11986–11993
 41. Kohno Y, Hayashi H, Takenaka S, Tanaka T, Funabiki T, Yoshida S. Photo-enhanced reduction of carbon dioxide with hydrogen over Rh/TiO₂. *Journal of Photochemistry and Photobiology A Chemistry*, 1999, 126(1–3): 117–123
 42. Zhou W, Guo J, Shen S, Pan J, Tang J, Chen L, Au C, Yin S. Progress in photoelectrocatalytic reduction of carbon dioxide. *Acta Physica Sinica*, 2020, 36(3): 1906048 (in Chinese)
 43. Xie F, Chen R, Zhu X, Liao Q, Ye D, Zhang B, Yu Y, Li J. CO₂ utilization: direct power generation by a coupled system that integrates photocatalytic reduction of CO₂ with photocatalytic fuel cell. *Journal of CO₂ Utilization*, 2019, 32: 31–36
 44. Chen M, Wu J, Lu C, Luo X, Huang Y, Jin B, Guo H, Zhang X, Argyle M, Liang Z. Photoreduction of CO₂ in the presence of CH₄ over g-C₃N₄ modified with TiO₂ nanoparticles at room temperature. *Green Energy & Environment*, 2021, in press